

Neural Multi-Atlas Label Fusion: Application to Cardiac MR Images

Heran Yang^a, Jian Sun^{a,b,*}, Huibin Li^{a,b}, Lisheng Wang^c, Zongben Xu^{a,b}

^a*School of Mathematics and Statistics, Xi'an Jiaotong University, China*

^b*National Engineering Laboratory for Big Data Algorithm and Analysis Technology, China*

^c*Department of Automation, Shanghai Jiaotong University, China*

Abstract

Multi-atlas segmentation approach is one of the most widely-used image segmentation techniques in biomedical applications. There are two major challenges in this category of methods, *i.e.*, atlas selection and label fusion. In this paper, we propose a novel multi-atlas segmentation method that formulates multi-atlas segmentation in a deep learning framework for better solving these challenges. The proposed method, dubbed deep fusion net (DFN), is a deep architecture that integrates a feature extraction subnet and a non-local patch-based label fusion (NL-PLF) subnet in a single network. The network parameters are learned by end-to-end training for automatically learning deep features that enable optimal performance in a NL-PLF framework. The learned deep features are further utilized in defining a similarity measure for atlas selection. By evaluating on two public cardiac MR datasets of SATA-13 and LV-09 for left ventricle segmentation, our approach achieved 0.833 in averaged Dice metric (ADM) on SATA-13 dataset and 0.95 in ADM for epicardium segmentation on LV-09 dataset, comparing favorably with the other automatic left ventricle segmentation methods. We also tested our approach on Cardiac Atlas Project (CAP) testing set of MICCAI 2013 SATA Segmentation Challenge, and our method achieved 0.815 in ADM, ranking highest at the time of writing.

Keywords: Multi-atlas label fusion, left ventricle segmentation, deep fusion net, atlas selection.

1. Introduction

As one of the most successful medical image segmentation techniques, multi-atlas segmentation (MAS) approach has been applied to various medical image segmentation tasks, including segmentation of abdominal anatomy (Tong et al., 2015; Wang et al., 2014; Wolz et al., 2013; Xu et al., 2015), cardiac ventricle (Xie et al., 2015; Bai et al., 2015, 2013; Zhuang and Shen, 2016), brain (Wu

*Corresponding author

Email address: jiansun@mail.xjtu.edu.cn (Jian Sun)

et al., 2014; Asman and Landman, 2013; Coupé et al., 2011; Duc et al., 2013; Artaechevarria et al., 2009; Sanroma et al., 2014; Wang et al., 2013; Cardoso et al., 2013; Asman et al., 2015), etc.

Given an image to be segmented, *i.e.*, a *target image*, multi-atlas segmentation methods utilize multiple *atlases*, *i.e.*, a number of images from multiple subjects with segmentation labels delineated by experts, to estimate the segmentation label of target image, *i.e.*, *target label*. Typically, multi-atlas segmentation methods first register atlas images to the target image, and then the corresponding warped atlas labels are combined to estimate the target label by a label fusion procedure (Iglesias and Sabuncu, 2015). To raise computational efficiency or improve final segmentation accuracy, multi-atlas segmentation methods employ an atlas selection procedure to select a few warped atlas images most similar to the target image, and only the labels of these selected images are utilized in the label fusion procedure (Aljabar et al., 2009). For a comprehensive review on multi-atlas segmentation methods, please refer to Iglesias and Sabuncu (2015).

A large body of literatures on multi-atlas segmentation focuses on the label fusion procedure. One typical label fusion strategy is weighted voting, where the label of each target voxel is determined by weighted average of the labels of corresponding voxels in warped atlas images. Local label fusion methods determine the voxel-wise fusion weights by local intensity-based similarities between the target and atlas voxels (Artaechevarria et al., 2009; Makropoulos et al., 2014). To account for possible registration errors, Coupé et al. (2011) proposed to fuse labels of all voxels in a non-local search window or volume around the registered atlas voxel for predicting the target label. This category of methods (Bai et al., 2015; Iglesias and Sabuncu, 2015; Wang et al., 2014) is commonly named as *non-local patch-based label fusion*. Moreover, statistical fusion methods were proposed to estimate the fusion weights by integrating models of rater performance (Cardoso et al., 2013; Asman and Landman, 2013; Warfield et al., 2004). Instead of using weighted voting strategy, sparsity-based dictionary learning (Tong et al., 2015) and matrix completion (Sanroma et al., 2015) methods predict target labels by representing image and label patch pairs using sparse regularization or low rank constraint. These related methods commonly use intensities or hand-crafted features for representing atlas and target voxels / patches to measure atlas-to-target similarity. A fundamental question is that whether we can automatically learn the features of atlas and target images directly aiming at achieving optimal label fusion performance.

Atlas selection, another important issue in multi-atlas segmentation, aims at selecting the most relevant atlases, which is generally achieved by ranking the atlases according to their similarities to the target image. The traditional methods rank atlases using intensity-based similarity measures, *e.g.*, normalized mutual information (Studholme et al., 1999; Collignon et al., 1995). Other well designed measures for atlas selection include the distance between transformations (Commowick et al., 2009), registration consistency (Heckemann et al., 2009), *etc.* Machine learning methods were also introduced to learn similarity measures for atlas selection, *e.g.*, manifold learning (Duc et al., 2013), ranking

SVM (Sanroma et al., 2014), *etc.* For atlas selection, how to design image features to measure the atlas-to-target image similarity for relevant atlas selection is also a fundamental task.

This work aims at designing a feature learning-based approach for better achieving label fusion and atlas selection in multi-atlas segmentation. We propose a novel multi-atlas segmentation method by reformulating non-local patch-based label fusion (NL-PLF) method (Coupé et al., 2011; Bai et al., 2015) to be a deep neural network (Krizhevsky et al., 2012). As shown in Fig. 1, the network is comprised of a *feature extraction subnet* for extracting deep features of each voxel in atlas and target images, and a *non-local patch-based label fusion subnet* (NL-PLF subnet) for fusing the warped atlases based on the extracted deep features. Our proposed deep fusion net relies on atlas-to-target image registration, and the net concentrates on learning deep features for fusing these warped labels using NL-PLF by an end-to-end training strategy. More specifically, the feature extraction subnet is learned to embed image into a deep feature space in which the feature similarity well reflects the label similarity, and then these deep features are utilized in NL-PLF subnet to compute the label fusion weights for achieving optimal segmentation performance in a NL-PLF framework. The learned deep features for label fusion can also be taken as the features for measuring atlas-to-target image similarity in atlas selection.

To the best of our knowledge, this is the first work accomplishing registration-based multi-atlas segmentation in a deep learning framework. The traditional non-local patch-based label fusion method relies on hand-crafted features, *e.g.*, intensities (Coupé et al., 2011), contextual features (Bai et al., 2015), for computing label fusion weights. Our approach takes advantage of the strong feature learning ability of deep neural network to learn optimal image features for label fusion in multi-atlas segmentation. This is achieved by our specially designed network architecture integrating the modules of feature learning and label fusion in an end-to-end learning framework.

We apply the proposed deep fusion net to left ventricle (LV) segmentation from short-axis cardiac MR images (Petitjean and Dacher, 2011), and achieved competitive results on two publicly available cardiac MR datasets, *i.e.*, MICCAI 2013 SATA Segmentation Challenge (SATA-13) dataset ¹ (Landman and Warfield, 2013) and MICCAI 2009 LV Segmentation Challenge (LV-09) dataset ² (Radau et al., 2009). Our approach achieved 0.833 in averaged Dice metric (ADM) on SATA-13 dataset and 0.95 in ADM for epicardium segmentation on LV-09 dataset. On the Cardiac Atlas Project (CAP) testing set of MICCAI 2013 SATA Segmentation Challenge, our method achieved 0.815 in Dice metric, ranking highest on this dataset at the time of writing.

Note that a preliminary version of this work was published in Yang et al. (2016). Compared with the conference paper, this journal paper presents the following extensions. (1) We more comprehensively discuss on the motivations

¹<https://www.synapse.org/#!Synapse:syn3193805/wiki/217780>

²https://smial.sri.utoronto.ca/LV_Challenge/Home.html

and details of the proposed method for better readability. (2) Our method is evaluated on additional dataset (LV-09 dataset) and compared with more segmentation methods, including the state-of-the-art deep learning methods. (3) More experiments are conducted to further explore the behaviors of the proposed method, *e.g.*, impact of atlas selection strategy, cross-dataset evaluation, *etc.*

1.1. Related work

1.1.1. Deep learning approach in medical image segmentation

In recent years, deep learning approach was widely applied in medical image segmentation, *e.g.*, vessel segmentation (Fu et al., 2016; Maninis et al., 2016; Khalaf et al., 2016), brain segmentation (Wachinger et al., 2017; Moeskops et al., 2016; Rajchl et al., 2017), *etc.* These methods commonly design different deep network structures considering backgrounds of specific problems, and directly learn the optimal network parameters for voxel-wise label prediction. For example, Havaei et al. (2017) proposed two-pathway cascaded deep networks with a two-phase training procedure for brain tumor segmentation. Chen et al. (2017) designed a multi-task fully convolutional neural network with multi-level contextual information for object instance segmentation from histology images. Ronneberger et al. (2015) proposed a data augmentation strategy by applying elastic deformations to the available training images, and designed a U-net architecture that consists of a contracting path to capture context and a symmetric expanding path enabling precise localization for cell segmentation in microscopic images. Moreover, Kamnitsas et al. (2017) proposed a multi-scale 3D convolutional neural network with two convolutional pathways for lesion segmentation in multi-modal brain MRI. In addition, some methods concentrate on defining proper loss functions for training deep segmentation networks on medical images. For example, Milletari et al. (2016) proposed a novel loss function based on Dice coefficient for prostate segmentation to deal with the strong imbalance between the number of foreground and background voxels. BenTaieb and Hamarneh (2016) designed a new loss for segmentations of histology glands to encode geometric and topological priors of containment and detachment. For a comprehensive review on deep learning in medical image analysis, please refer to Litjens et al. (2017).

1.1.2. Cardiac MR left ventricle segmentation

Accurately segmenting the LV from cardiac MR images is essentially important for quantitatively assessing the cardiac function in clinical diagnosis, which is still a challenging task due to large variation of LV in intensity levels, structural shapes, respiratory motion artifacts, partial volume effects, *etc.*

Multi-atlas segmentation approach is widely applied in LV segmentation. Bai et al. (2015) incorporated intensity, gradient and contextual information into an augmented feature vector for similarity measure in the non-local patch-based label fusion framework. Instead of only considering the corresponding atlas slice to the target image, Xie et al. (2015) fused the labels of all atlas slices in a neighborhood to produce a more accurate estimated target label.

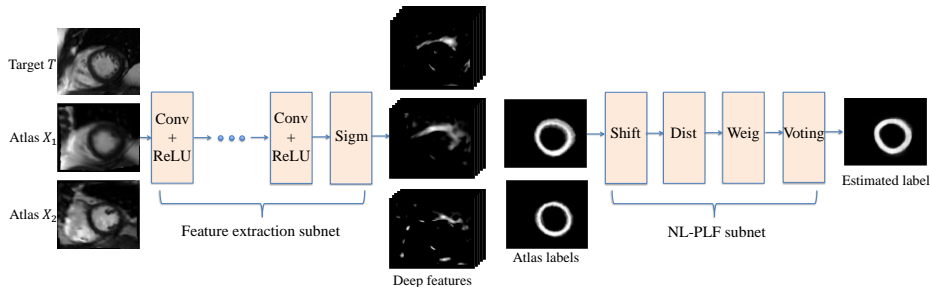


Fig. 1: The architecture of deep fusion net. A target image T and its warped atlas images X_i are first fed into a *feature extraction subnet* to extract deep features. These features and atlas labels are then sent to a *non-local patch-based label fusion (NL-PLF) subnet* for generating the estimated label of target image, *i.e.*, target label.

Wang et al. (2013) formulated the weighted voting as a problem of minimizing total expectation of labeling error, and pairwise dependency between atlases was modeled as a joint probability of two atlases making a segmentation error at a voxel. Due to the close connection between label fusion and registration, Bai et al. (2013) attempted to alternately perform patch-based label fusion and registration refinement.

In recent years, deep learning approach was also applied to LV segmentation. For example, Avendi et al. (2016) utilized convolutional neural networks to determine the region of interest (ROI) containing LV and stacked autoencoders to infer the LV segmentation mask. Then the segmentation mask was incorporated into level set model to produce the final segmentation result. Ngo et al. (2017) first estimated the ROI and an initial segmentation by deep belief network and Otsu’s thresholding, and then refined the initial segmentation by level set model. These two methods achieved high accuracies on MICCAI 2009 LV Segmentation Challenge dataset, but their performance largely relies on the post-processing by level set method. In these work, the segmentation results purely using deep networks are unsatisfactory (Avendi et al., 2016; Ngo et al., 2017; Guo et al., 2016) possibly due to insufficient labeled training data or limitation of designed network architecture, and the post-processing by level set method helps to refine the segmentation results to be continuous and connected.

Our proposed deep fusion net bridges the multi-atlas segmentation approach and deep learning approach. Compared with the traditional multi-atlas segmentation methods, our net also relies on atlas-to-target image registration. But instead of using hand-crafted features for label fusion, our net learns to extract deep features for computing optimal fusion weights in a NL-PLF framework. Compared with the common deep learning methods directly learning mapping from image to semantic labels, our network architecture is non-conventional and inspired by a registration-based multi-atlas label fusion strategy. With this novel deep architecture, our approach achieved improved results compared with the traditional multi-atlas segmentation methods and automatic deep learning methods on two cardiac MR image datasets, and the only deep learning method

surpassing our results depends on a strong manual prior (Ngo et al., 2017).

2. Deep Fusion Net for Multi-Atlas Segmentation

This section presents the proposed deep fusion net for multi-atlas segmentation, including the general framework, network architecture, training and testing procedures.

2.1. General framework

As a registration-based multi-atlas segmentation method, multiple atlas images are first registered to the target image by a non-rigid registration method, and then the corresponding atlas labels are warped to the target image using these transformations. Our proposed deep fusion net (DFN) is designed to fuse the warped atlas labels using discriminatively learned deep features. As shown in Fig. 1, deep fusion net consists of a feature extraction subnet, followed by a non-local patch-based label fusion (NL-PLF) subnet.

Feature extraction subnet: The feature extraction subnet is responsible for extracting dense deep features from target and atlas images, and all these images share the same feature extraction subnet. This subnet is learned to embed the input images into a deep feature space, in which the feature similarity between paired voxels are expected to better reflect the similarity of their labels. The extracted dense deep features are utilized by the following NL-PLF subnet for computing the label fusion weights using the deep feature similarity.

NL-PLF subnet: The NL-PLF subnet aims to fuse the warped atlas labels for predicting the target label. It implements a non-local patch-based label fusion strategy that predicts the target label by the weighted average of atlas labels within a search volume around the registered voxels. The effectiveness of this label fusion strategy relies on an effective measure of feature similarity for the fusion weight computation. This subnet takes the extracted deep features by feature extraction subnet as input, and accomplishes the non-local patch-based label fusion using the weights computed based on these extracted features.

The deep fusion net integrates the modules of feature extraction for feature embedding and label fusion for target label prediction. The network parameters are learned by an end-to-end training procedure minimizing a loss defined between network output and ground-truth target label. By enforcing that the estimated segmentation label should approximate the target label in training, the feature extraction subnet is discriminatively learned to extract deep features with feature similarity well representing the label similarity for computing the optimal label fusion weight.

In computer vision, siamese neural networks were proposed for learning deep feature embedding, and the learned feature similarity was utilized for patch matching (Zagoruyko and Komodakis, 2015), face recognition (Chopra et al., 2005; Schroff et al., 2015) and re-identification (Zheng et al., 2016), *etc.* Simi-

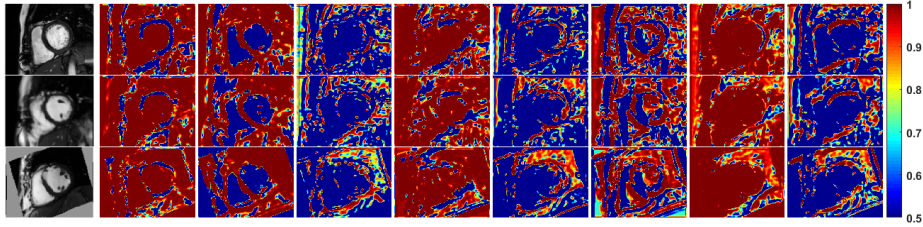


Fig. 2: Visualization of extracted features by learned feature extraction subnet. Top to bottom: a target image, two warped atlas images. Left to right: input image, first eight extracted feature maps.

larly, our feature extraction subnet aims to embed image patches³ into a deep feature space, in which the feature similarity is a meaningful measure of semantic label similarity. The deep feature similarity is further utilized to define label fusion weights for warped atlas label fusion or retrieve relevant atlases in atlas selection.

In the following sections 2.2 and 2.3, we will respectively introduce the architectures of feature extraction subnet and NL-PLF subnet.

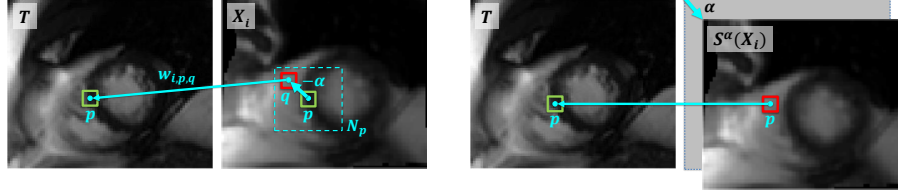
2.2. Feature extraction subnet

Assume that we are given a target image T and multiple atlases. After registering atlas images to the target image T , the pairs of warped atlas image and label map are denoted as $\{X_i, L(X_i)\}_{i=1}^K$, where X_i is the i -th warped atlas image, and $L(X_i)$ is the corresponding warped label map. K denotes the number of atlases. The feature extraction subnet is responsible for extracting dense deep features from images, including the target image T and warped atlas images $\{X_i\}_{i=1}^K$, and the extracted dense features are respectively denoted as $F(T)$ and $\{F(X_i)\}_{i=1}^K$.

As shown in Fig. 1, the feature extraction subnet consists of multiple repetitions of convolutional layer with ReLU activation function, and a final sigmoid layer for feature normalization. All input images of this subnet, including the target image and warped atlas images, share the same subnet. Figure 2 shows examples of extracted feature maps of one target image and two warped atlas images by the feature extraction subnet after training. These extracted features well describe different structures of the input images.

Convolutional block. The convolutional block aims at learning discriminative local patterns represented by filters from its input features. This block convolves the input features using a set of learnable filters $\{\mathcal{W}_{d'}\}_{d'=1}^{D'}$, followed by non-linear activation function. Each filter $\mathcal{W}_{d'} \in \mathbb{R}^{w_f \times w_f \times D}$ is a third-order tensor, where D' is the number of filters, D denotes the number of *feature maps* in input features, and $w_f \times w_f$ is the size of filters. Given the input features

³The image patch size is determined by the receptive field of feature extraction subnet.



(a) Non-local patch-based label fusion: each patch, e.g., patch around q , in a window N_p of T and q of X_i in (a) equals to feature distance between p of T and q of X_i in (a) equals to feature distance of T and $S^\alpha(X_i)$ at p .

Fig. 3: Illustration of non-local patch-based label fusion and shift operation.

$G^{l-1}(X) \in \mathbb{R}^{M \times N \times D}$ of image X , the l -th convolutional block outputs features $G^l(X) \in \mathbb{R}^{(M-w_f+1) \times (N-w_f+1) \times D'}$, whose d' -th feature map, denoted as $g_{d'}^l$, can be written as

$$g_{d'}^l = \varphi(\mathcal{W}_{d'} * G^{l-1}(X) + b_{d'}^l), \quad (1)$$

where $*$ is the 3-D convolution operator, and $b_{d'}^l$ is the bias term. φ is a rectified linear unit (ReLU) function (Nair and Hinton, 2010): $\varphi(x) = \max(0, x)$.

Sigmoid layer. The feature extraction subnet is completed with a final sigmoid layer. The sigmoid layer can suppress the large feature magnitude and non-linearly map the extracted features to a limited range within $[0.5, 1)$, which is expected to enforce robustness of deep fusion net to different image contrasts. The experimental evaluation on the necessity of this sigmoid layer is presented in section 4.5.1. Given input features $G(X) \in \mathbb{R}^{M \times N \times D}$ of image X , each element $f_{m,n,d}$ in the transformed features $F(X) \in \mathbb{R}^{M \times N \times D}$ can be computed via processing each element $g_{m,n,d}$ of $G(X)$ by

$$f_{m,n,d} = \frac{1}{1 + e^{-g_{m,n,d}}}, \quad (2)$$

where (m, n, d) denotes the three-dimensional index of element in input or transformed features.

2.3. Non-local patch-based label fusion subnet

This subnet is a deep architecture implementing non-local patch-based label fusion strategy on top of feature extraction subnet. As shown in Fig.1, our NL-PLF subnet consists of *shift layer*, *distance layer*, *weight layer* and *voting layer*, and finally outputs the estimated label of target image.

Figure 3(a) shows the idea of non-local patch-based label fusion strategy. For simplicity, we use the notation p to denote a pixel's spatial position instead of (m, n) . To account for atlas-to-target image registration errors, all the pixels in a search window around the pixel p in warped atlas images $\{X_i\}_{i=1}^K$ are considered as the potential corresponding pixels for the pixel p in target image

T . Therefore, the labels of these pixels in atlas images are fused to produce the estimated target label at pixel p .

Contrary to the hand-crafted features adopted in Bai et al. (2015), deep fusion net computes the fusion weights using the deep features extracted by the feature extraction subnet. The fusion weights are defined as the normalized distances between these deep features, and the normalization is accomplished by softmax operator, enforcing that the summation of all fusion weights related to each pixel p in target image T is one. More precisely, the fusion weight of pixel q in warped atlas image X_i for predicting the label of pixel p in target image T is determined as

$$w_{i,p,q}(\Theta) = \frac{\exp(-\|F_p(T; \Theta) - F_q(X_i; \Theta)\|_2^2)}{\sum_j \sum_{q' \in N_p} \exp(-\|F_p(T; \Theta) - F_{q'}(X_j; \Theta)\|_2^2)}, \quad (3)$$

where Θ is the network parameters, *i.e.*, filters and biases, in feature extraction subnet. $F_p(T; \Theta)$ is the extracted feature vector of image T at pixel p , and N_p is the search window around pixel p .

Hence, the estimated label of pixel p in target image T can be written as

$$\hat{L}_p(T; \Theta) = \sum_i \sum_{q \in N_p} w_{i,p,q}(\Theta) L_q(X_i), \quad (4)$$

where $L_q(X_i)$ is the label of atlas image X_i at pixel q .

The objective of learning deep fusion net is to enforce that the estimated label of target image T in Eqn.(4) should approximate the ground-truth target label $L(T)$ as close as possible. Therefore, a *loss layer* for measuring the approximation error is defined as a L_2 loss:

$$E(\hat{L}(T; \Theta), L(T)) = \frac{1}{P} \sum_p \|\hat{L}_p(T; \Theta) - L_p(T)\|_2^2, \quad (5)$$

where P denotes the number of pixels in target image T . Our task in network training is to minimize this loss function on a training set *w.r.t.* the network parameters Θ using back-propagation. For notational convenience, we will omit network parameters Θ in the rest of paper.

Based on the formula of label prediction in Eqn. (4), our network output $\hat{L}_p(T)$ is very often a hard 0 or 1 rather than the soft probability in $(0, 1)$ of a standard soft-max classifier, and we expect the L_2 loss to be more computationally stable and smoother to optimize than the commonly used cross-entropy loss. Please refer to section 1 of appendix for gradient computations using L_2 and cross-entropy losses. In preliminary experiments, we also tried several different loss functions, *e.g.*, L_1 , hinge, Dice and log losses, and L_2 loss behaved marginally better. Please refer to section 4.5.2 for these experiments.

To incorporate Eqn.(3) into the neural network as a differentiable function, we decompose the computation of the fusion weights into several successive simple operations, modeled as *shift layer*, *distance layer* and *weight layer*. Each operation and the gradient of its output *w.r.t.* input can be easily calculated

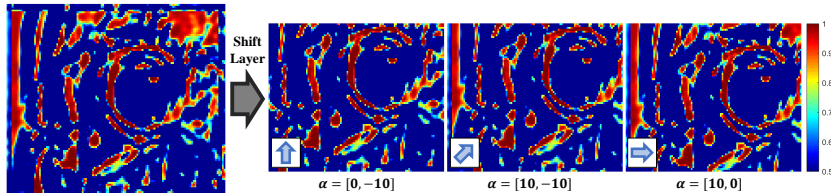


Fig. 4: Illustration of shift operator S^α with three different values of α . For one feature map (left), these shift operators shift it along different vectors α and generate shifted feature maps (right). Note that the areas going out of the border are carefully cropped.

using standard deep-learning libraries. Figure 3 shows our motivation for this decomposition in detail. Instead of directly computing the feature distance of pixel p in target image T and pixel q in atlas image X_i , shown in Fig. 3(a), we can equivalently compute the per-pixel feature distance at the pixel p between target image T and the shifted atlas image X_i by the shift vector $\alpha = p - q$, as shown in Fig. 3(b). Suppose that the search window width is $2t + 1$. To calculate the fusion weights using Eqn.(3) in deep networks, we first shift each feature map of X_i by each shift vector α within the non-local region $R_{nl} = \{(u, v) \in \mathbb{Z}^2 \mid -t \leq u, v \leq t\}$ using a *shift layer*, then compute the pixel-wise feature distances using a *distance layer*, and finally transform these distances to fusion weights using a *weight layer*.

2.3.1. Shift layer

The shift layer spatially shifts the extracted features or label map of each atlas image. Given the extracted features $F(X_i) \in \mathbb{R}^{M \times N \times D}$ of atlas image X_i , this layer generates $(2t + 1) \times (2t + 1)$ spatially shifted features along each shift vector $\alpha \in R_{nl}$. Each output of the shift layer can be written as $S^\alpha(F(X_i))$, where S^α denotes the shift operator with a shift vector α . Figure 4 illustrates an example of shift operator S^α with different values of α on one feature map. Each shift operator S^α is actually an identity function between shifted features, and thus the gradients can be propagated back accordingly. Note that careful cropping is needed for areas going out of the border due to shift operators.

2.3.2. Distance layer

The distance layer computes the pixel-wise feature distance at each pixel p between shifted features $S^\alpha(F(X_i))$ of atlas X_i and target's features $F(T)$ as

$$D_p^\alpha(T, X_i) = \|S_p^\alpha(F(X_i)) - F_p(T)\|_2^2, \quad (6)$$

where $S_p^\alpha(F(X_i))$ denotes the feature vector of shifted features $S^\alpha(F(X_i))$ at pixel p . It is defined as the pixel-wise L_2 distance, and the gradient of this layer can be simply derived *w.r.t.* both $S^\alpha(F(X_i))$ and $F(T)$.

2.3.3. Weight layer

The weight layer maps the feature distances to fusion weights using softmax operation. The fusion weight of pixel q ($q = p - \alpha, \alpha \in R_{nl}$) in atlas image X_i

for predicting the label of pixel p in target image T can be written as

$$w_{i,p,q} = w_p^\alpha(X_i) = \frac{e^{-D_p^\alpha(T, X_i)}}{\sum_j \sum_{\alpha' \in R_{nl}} e^{-D_p^{\alpha'}(T, X_j)}}. \quad (7)$$

This softmax operation is a common layer in architecture of deep networks, and the gradient of this layer *w.r.t.* the input $D_p^\alpha(T, X_k)$ can be easily derived (Goodfellow et al., 2016), where k is any atlas index.

2.3.4. Voting layer

The voting layer estimates the label of target image T at pixel p by

$$\hat{L}_p(T) = \sum_i \sum_{\alpha \in R_{nl}} w_p^\alpha(X_i) S_p^\alpha(L(X_i)). \quad (8)$$

As a linear operation, the gradient of this layer can be easily derived *w.r.t.* the input $w_p^\alpha(X_i)$.

Summary: The non-local patch-based label fusion subnet successively processes the extracted features and warped atlas labels by *shift*, *distance*, and *weight layers* to output fusion weights, which are then utilized by *voting layer* to estimate the target label. This subnet implements Eqn.(3) by using the above simple layers, and the gradients of these layers can be easily calculated using standard deep-learning libraries.

2.4. Deep fusion net for binary and multi-class segmentation

The deep fusion net can be adapted to both tasks of binary and multi-class segmentation. This can be uniformly achieved by representing the segmentation label L_p of target or warped atlas pixel p using probability vector in the voting layer. Suppose that there are C classes for segmentation, the segmentation label of pixel p can be represented by $L_p = (a_1, \dots, a_C)^\top$ where $a_i \geq 0$ and $\sum_i a_i = 1$. a_i represents the probability of pixel p belonging to class i . For binary segmentation, $L_p = (a, 1 - a)^\top$ where a represents the probability of pixel p belonging to object of interest.

2.5. Network training

We learn the network parameters Θ by minimizing the loss in Eqn.(5) *w.r.t.* Θ using back-propagation. Given a number of atlases for training, each atlas is selected as the target image in turn, and then the remaining atlases are registered to this target image as the warped atlases. Suppose that i -th atlas is picked as the target image T with ground-truth label $L(T)$, the corresponding warped atlases are denoted by $\mathcal{A}_i = \{X_j, L(X_j) | j = 1, 2, \dots, K, j \neq i\}$, where K is the total number of atlases.

We use stochastic gradient descent in training, and each triplet of $(\mathcal{A}_i, T, L(T))$ is taken as a batch. Instead of using all warped atlases within \mathcal{A}_i in each batch, which may require a large GPU memory and long training time, we randomly

sample K_0 ($K_0 = 5$) warped atlases for training, according to a distribution proportional to the normalized mutual information between warped atlas images $\{X_j | j = 1, 2, \dots, K, j \neq i\}$ and target image T . This random atlas selection strategy enriches the diversity of warped atlases for target image at training phase. Since there may be discrepancy between distributions of training and testing data, this strategy may improve the generalization ability of deep fusion net for testing data. We will evaluate the atlas selection strategy at training phase in section 4.6. Many randomized techniques were also proposed in deep learning to improve network generalization ability, *e.g.*, dropout (Srivastava et al., 2014), data augmentation (Vincent et al., 2008), *etc.*

2.6. Network testing

At testing phase, the learned deep fusion net loads a test sample (a target image and its warped atlases) and outputs the estimated target label. Similar to multiple atlas selection approaches (Sanroma et al., 2014; Duc et al., 2013; Aljabar et al., 2009), we only pick a few most similar atlases for the target image in label fusion, which is an atlas selection problem. As discussed in section 2.1, feature extraction subnet actually learns an embedding space at training process, in which pixel-wise L_2 feature distance within distance layer corresponds to image similarity. We can naturally define a deep feature distance between a target image T and its warped atlas image X_i as

$$d_F(T, X_i) = \|F(T) - F(X_i)\|_F^2, \quad (9)$$

where $F(\cdot)$ is the extracted features using well-trained feature extraction subnet at training process. At testing phase, we take the top- k atlases with smallest deep feature distances as the selected atlases for a target image, which are then fed into the learned deep fusion net to estimate the target label. Note that the number k of selected atlases at testing process does not need to be same as K_0 used at training phase. In fact, one could intuitively expect that K_0 at training phase would make the features to be learned in a way that the network operates best at testing phase with $k = K_0$. However, we show empirically in section 4.6 that a larger number k at testing phase would generally produce better segmentation accuracies. This happens possibly because of the random atlas selection strategy utilized at training phase, which largely extends the diversity of warped atlases for target image at training phase and enables the network to utilize more warped atlases at testing process.

3. Implementation details and computational requirements

Our current implementation is based on the MatConvNet library ⁴, and all experiments are performed on a Dell Precision T7910 workstation with GeForce

⁴<http://www.vlfeat.org/matconvnet/>

GTX TITAN X (12GB) on an Ubuntu platform. In the current study, our proposed method processes cardiac MR images slice by slice, and the GPU memory requirement for processing one target image is about $O(MNDK_0(2t+1)^2)$. The averaged size of target images for numerical experiments in section 4 is about 110×140 for SATA-13 dataset and 135×155 for LV-09 dataset. In practice, for a target image in size of 120×140 with $K_0 = 5$, a deep fusion net with network parameters in section 4.3 requires about 4GB GPU memory for one forward and backward processes, which respectively take about 0.30 second and 0.31 second. In this case, the maximum allowed number of selected atlases K_0 for training is up to 42 in our computational platform.

4. Experiments

In this section, we evaluate the performance of deep fusion net on two cardiac MR datasets for left ventricle (LV) segmentation. In the following paragraphs, we will compare our method with other segmentation methods and further investigate the performance of our deep fusion net with variants of architecture, loss, atlas selection strategy, cross-dataset evaluation on these two datasets. In appendix, we also provide additional experiments, including justification of the effectiveness of learned deep features as similarity measure, and all the p -values appearing in the following paragraphs.

4.1. Datasets

4.1.1. SATA-13 dataset

The MICCAI 2013 SATA Segmentation Challenge (SATA-13) provides a cardiac dataset for LV segmentation. The samples in this dataset are randomly selected from DETERMINE (Defibrillators to Reduce Risk by Magnetic Resonance Imaging Evaluation) in Cardiac Atlas Project (CAP). The cardiac MR images are acquired using the steady-state free precession (SSFP) pulse sequence, and each image is acquired during a breath-hold of 8-15 seconds duration. Sufficient short-axis slices are obtained to cover the whole heart, and the MR parameters vary between cases. Typically, each cine image sequence has about 25 frames, and each frame has about 10 slices. The size of slice ranges from 138×192 to 512×512 . The slice thickness is less than 10 mm, and the gap between slices is less than 2 mm.

The SATA-13 dataset includes 83 training subjects and 72 testing subjects. The ground-truth myocardium segmentation masks for all frames in training subjects are provided, while we evaluate our deep fusion net only on end-diastole (ED) frame, as a common practice in the literature (Petitjean and Dacher, 2011; Shi et al., 2014). The experiment is performed over 83 training subjects using 5-fold cross validation, *i.e.*, one fifth of training subjects are taken as validation set and the remaining four fifths of subjects are taken for learning deep fusion net in each fold. The averaged 3D Dice metric (ADM) and averaged 3D Hausdorff distance (AHD) over the validation sets in five folds are taken as the final accuracies. For one subject in validation sets, assume that Ω_{gt} and Ω_{et}

are respectively its ground-truth and estimated segmentations represented by sets of pixels labeled as object of interest, the Dice metric (DM) and Hausdorff distance (HD) are defined as $DM(\Omega_{gt}, \Omega_{et}) = \frac{2|\Omega_{gt} \cap \Omega_{et}|}{|\Omega_{gt}| + |\Omega_{et}|}$ and $HD(\Omega_{gt}, \Omega_{et}) = \max \left(\max_{p \in \Omega_{gt}} \left(\min_{q \in \Omega_{et}} d(p, q) \right), \max_{q \in \Omega_{et}} \left(\min_{p \in \Omega_{gt}} d(p, q) \right) \right)$, where $|\cdot|$ denotes the number of elements in a set and $d(p, q)$ denotes the Euclidean distance between coordinates of pixels p and q . The Hausdorff distance is computed in spatial resolution of millimeter obtained from the DICOM file.

4.1.2. LV-09 dataset

The MICCAI 2009 LV Segmentation Challenge (LV-09) dataset (Radau et al., 2009) is provided by Sunnybrook Health Sciences Center, and contains 45 subjects with expert annotations, respectively in subsets of “training”, “testing” and “online”. The cardiac cine-MR short-axis images are acquired using SSFP pulse sequence with a 1.5T GE Signa MRI. All images are obtained during 10-15 seconds of breath holding with a temporal resolution of 20 cardiac phases over the heart cycle. Each subject contains all slices at end-diastole (ED) and end-systole (ES) frames, and each frame contains 6-12 short-axis images obtained from the atrioventricular ring to the apex (thickness = 8 mm, gap = 8 mm, FOV = 320 × 320 mm, matrix = 256 × 256). Both endocardial and epicardial contours are drawn by experienced cardiologists in all slices at ED frame, while only endocardial contours are given at ES frame.

In the experiment, as in Avendi et al. (2016), we utilize 15 training subjects for learning deep fusion net, and 30 subjects in testing and online sets for evaluating the performance. The standard evaluation scheme of MICCAI 2009 LV Segmentation Challenge (Radau et al., 2009) is utilized in our comparison, which is based on the following three measures: 1) percentage of “good” contours, 2) averaged Dice metric (ADM) of the “good” contours, and 3) averaged perpendicular distance (APD) of the “good” contours. A contour is classified as “good” if APD is less than 5 mm. The Dice metric and perpendicular distance are calculated for each 2D slice separately, and the evaluation measures (*i.e.*, “Good” percentage, ADM and APD) are averaged over all slices within ED and ES frames of all subjects in testing or online sets.

4.2. Preprocessing

Before starting to learn deep fusion net, atlas images are registered to the target image using ITK software package ⁵, and we utilize two different registration frameworks to test the robustness of our proposed method.

Landmark-based (LB) registration: Each atlas subject is warped to the target subject using landmark-based registration with 3D affine transformation, and five landmarks are manually labeled at both atlas and target images, as in Bai et al. (2013). These landmarks are also used to crop the region of interest (ROI) from complex backgrounds to reduce the computational cost of registration. To

⁵<http://www.itk.org/>

compensate for the potential inter-slice shift, 2D B-spline registration is then utilized on each pair of slices in atlas and target subjects respectively.

Landmark-free (LF) registration: The ROI is cropped by a bounding box on each subject determined by two corner points, and then each atlas subject is warped to the target subject by 3D affine registration without using any landmarks. Normalized mutual information (NMI) is taken as the similarity metric. At last, 2D affine registration and 2D B-spline registration are successively applied to each slice for reducing the potential inter-slice shift.

Generally speaking, LB registration framework would produce more accurate results due to the guidance of landmarks. In each process of registration, with the estimated motion between atlas and target images, each atlas label is warped to provide an estimate for the target label using the corresponding motion field. All the warped estimates for target label are fused by deep fusion net to generate a final prediction of the target label.

4.3. Parameter settings

Empirically, we fix the learning rate of deep fusion net to 5×10^{-7} . Unless otherwise stated, the numbers of selected atlases at training and testing phases, *i.e.*, K_0 and k , are respectively 5 and 10, and the size of search window in the shift layer is 7×7 . As for the feature extraction subnet, we utilize 4 convolutional layers with strides of 1, and these layers respectively have 64 filters in size of $5 \times 5 \times 1$, 64 filters in size of $5 \times 5 \times 64$, 128 filters in size of $5 \times 5 \times 64$, and 128 filters in size of $5 \times 5 \times 128$.

4.4. Segmentation accuracy

4.4.1. SATA-13 dataset

For SATA-13 dataset, we compare the segmentation accuracy of deep fusion net with the results of majority voting (MV), patch-based segmentation (PB) (Coupé et al., 2011), as well as SVM-based segmentation with augmented features (SVMAF) (Bai et al., 2015). Another version of deep fusion net which uses normalized mutual information (NMI) as similarity measure for atlas selection at testing process, denoted as DFN_NMI, is also included in the comparison. The results of MV, PB and SVMAF are reproduced by the published codes ⁶ using the same parameter settings in Bai et al. (2015). The segmentation accuracy is evaluated by averaged Dice metric (higher value means better performance) and averaged Hausdorff distance (lower value means better performance) of the myocardium across ED frame and all the testing subjects in 5-fold cross validation. A paired-samples t-test is conducted to compare the performance of segmentation approaches.

Table 1 reports the quantitative segmentation accuracies of different methods using LB or LF registrations introduced in section 4.2. The experimental results show that our DFN achieves better performance than the methods of MV,

⁶<http://wp.doc.ic.ac.uk/wbai/software/>

Method	Registration framework	Averaged Dice metric	Averaged Hausdorff distance
CNN	-	0.695(0.092)	52.33(11.59)
MV	LB	0.747(0.057)	12.16(3.87)
PB	LB	0.761(0.056)	12.11(3.86)
SVMAF	LB	0.777(0.057)	17.31(4.40)
DFN	LB	0.833(0.039)	11.35(3.53)
DFN	LF	0.815(0.044)	18.33(8.98)
DFN_NMI	LB	0.831(0.039)	11.98(3.84)
DFN_NMI	LF	0.802(0.051)	27.00(12.75)
DFN(crossDS)	LB	0.815(0.040)	11.76(3.70)
DFN_NMI(crossDS)	LB	0.809(0.040)	12.46(4.19)

Table 1: Myocardium segmentation accuracies of different methods on SATA-13 dataset. Each cell is formatted as “mean (standard deviation)”. “LB”, “LF” and “-” respectively denote landmark-based registration, landmark-free registration and registration-free method.

PB and SVMAF in both ADM (p -value < 0.001) and AHD (p -value < 0.05) when using LB registration. In addition, our DFN and DFN_NMI using LF registration obtain higher accuracies in ADM than these compared methods of SVMAF, PB, MV, CNN using LB registration (p -value < 0.001). As for similarity measures in atlas selection, by comparing DFN (using deep features for atlas selection) with DFN_NMI (using NMI for atlas selection), our defined deep feature-based atlas selection works significantly better in terms of both two metrics (p -value < 0.001) when using LF registration, improving ADM from 0.802 to 0.815 and AHD from 27.00 to 18.33. However, this improvement when using landmark-based (LB) registration is marginal by comparing DFN and DFN_NMI with LB registration, possibly because LB registration achieves better registration quality decreasing the dependency of segmentation accuracy on a better atlas selection strategy.

Convolutional neural network (CNN) is also included in this comparison to evaluate the effect of NL-PLF subnet, and we restrict that the CNN and our DFN have identical network capacity of feature extraction, *i.e.*, the compared CNN in Table 1 has the same feature extraction subnet as ours in section 4.3, which is then followed by a convolutional layer and a softmax layer to output the target label. The meta-parameters of CNN, *e.g.*, learning rate, are reconfigured to the best of our abilities. Experimental results show that our DFN performs significantly better than CNN in all metrics (p -value < 0.001), indicating the effectiveness of NL-PLF subnet.

Figure 5 compares the segmentation accuracies in the box-plot, showing that our DFN based on LB registration achieves significantly higher median values than the compared methods in ADM, and is marginally better in AHD compared with PB and MV. Figure 6 shows visual examples of the segmentation results by different methods on the basal, mid-ventricular and apical slices from a testing

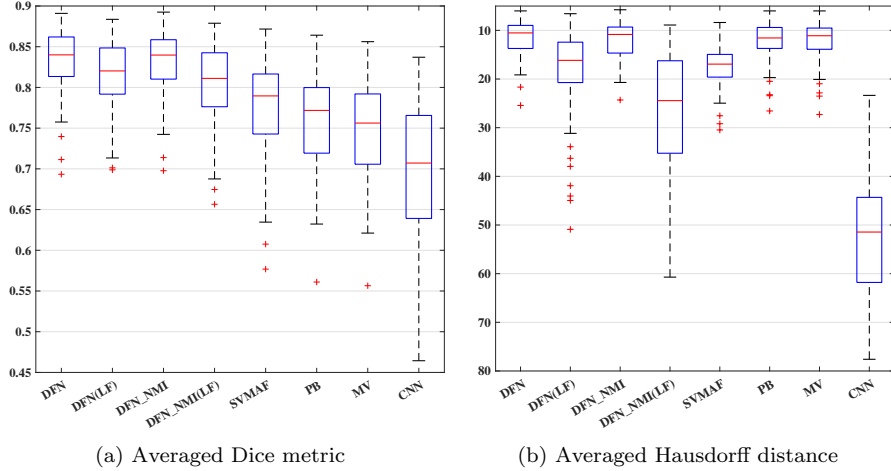


Fig. 5: Comparison of myocardium segmentation accuracies for different methods on SATA-13 dataset in terms of (a) ADM and (b) AHD. The red central mark of the box is the median and the edges are the 25th and 75th percentiles, while the red plus signs represent outliers.

subject.

Furthermore, to compare with other state-of-the-art methods, we trained a deep fusion net on Cardiac Atlas Project (CAP) training set of MICCAI 2013 SATA Segmentation Challenge and tested its performance on CAP testing set of the challenge, whose ground-truth segmentations are unknown to challenge participants. We submitted our segmentation results to the challenge website, and the corresponding testing accuracies were evaluated by the website and

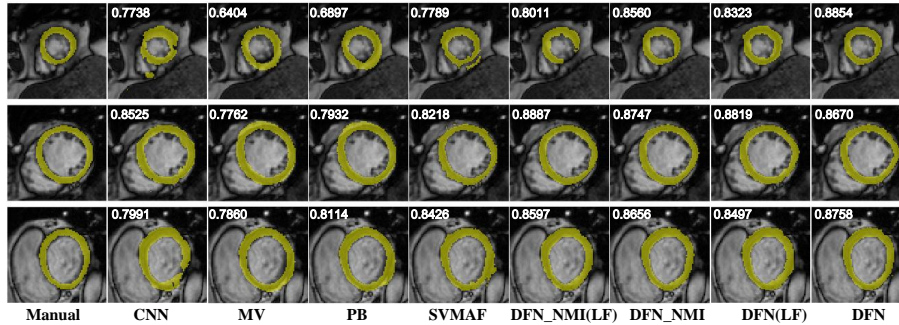


Fig. 6: Visual comparison of myocardium segmentation results using different methods on SATA-13 dataset. Please refer to the electronic version for better comparison. Top to bottom: the basal, mid-ventricular and apical slices from the same testing subject. Left to right: manual labeling, convolutional neural network (CNN), majority voting (MV), patch-based method (PB), SVM segmentation with augmented features (SVMAF), DFN_NMI using LF registration, DFN_NMI, DFN using LF registration, and DFN. The small white text on each sub-image is the corresponding 2D Dice metric value.

published on its leaderboard ^{7,8}. Our proposed deep fusion net based on LB registration (referred as DeepMAS_LB) achieved 0.815 in Dice metric, ranking first among the submitted results at the time of writing.

4.4.2. LV-09 dataset

For LV-09 dataset, we respectively compare the epicardium and endocardium segmentation accuracies of the testing and online sets in Tables 2 and 3. Similar to Ngo et al. (2017), both ED and ES frames are evaluated to measure accuracies for endocardium segmentation, while only ED frame is evaluated for the epicardium segmentation. Besides the traditional multi-atlas segmentation methods, we also compare two recent deep learning-based methods that achieve state-of-the-art results on this dataset, *i.e.* the combined stacked autoencoder and level set method (SAELS) (Avendi et al., 2016) and the combined deep belief network and level set method (DBNLS) (Ngo et al., 2017). Both SAELS and DBNLS first utilize deep network to estimate an initial segmentation result, which is then refined by level set approach to produce a final estimation. More exactly, DBNLS respectively trains four DBNs for epicardium or endocardium at ED or ES frame, and SAELS respectively trains two networks for large-contour or small-contour images on endocardium segmentation. In our experiments, we try two different versions of network training: first, three different deep fusion nets are respectively trained for epicardium at ED, endocardium at ED and endocardium at ES; second, one multi-class deep fusion net (indicated by “multi” in tables) is trained for epicardium and endocardium at ED, and one deep fusion

Method	Registration Framework	“Good” percentage		Epicardium ADM		Epicardium APD	
		Testing	Online	Testing	Online	Testing	Online
MV	LB	94.60(8.17)	92.34(13.16)	0.93(0.02)	0.92(0.02)	2.57(0.41)	2.80(0.42)
PB	LB	94.60(8.17)	92.34(13.16)	0.93(0.02)	0.92(0.02)	2.54(0.41)	2.77(0.43)
SVMAF	LB	95.43(8.03)	84.84(21.74)	0.93(0.01)	0.93(0.01)	2.85(0.50)	3.01(0.47)
DBNLS	-	94.65(6.18)	84.32(23.45)	0.93(0.02)	0.93(0.03)	2.08(0.60)	2.05(0.61)
DBNLS(semiauto)	-	100(0)	100(0)	0.94(0.01)	0.94(0.02)	1.73(0.28)	1.90(0.53)
DFN	LB	100(0)	93.62(13.55)	0.95(0.01)	0.95(0.01)	1.90(0.22)	1.98(0.27)
DFN	LF	78.90(20.58)	65.40(29.46)	0.94(0.01)	0.93(0.04)	2.55(0.80)	2.73(0.68)
DFN(multi)	LB	97.43(7.64)	96.26(8.19)	0.95(0.01)	0.95(0.01)	2.11(0.26)	2.15(0.46)
DFN_NMI	LB	98.67(3.52)	92.53(13.58)	0.96(0.01)	0.95(0.01)	1.88(0.18)	2.01(0.32)
DFN_NMI	LF	66.15(21.00)	50.54(27.29)	0.93(0.03)	0.93(0.03)	2.80(0.86)	2.91(0.79)
DFN_NMI(multi)	LB	97.43(7.64)	95.02(11.91)	0.95(0.01)	0.94(0.01)	2.15(0.27)	2.17(0.41)

Table 2: Epicardium segmentation accuracies of different methods on testing and online sets of LV-09 dataset, where only training set is used as training data. Each cell is formatted as “mean (standard deviation)”.

⁷Old website: <http://masi.vuse.vanderbilt.edu/submission/leaderboard.html>

⁸New website: <https://www.synapse.org/#!/Synapse:syn3193805/wiki/217788> (Last accessed: 10 July 2018)

Method	Registration Framework	“Good” percentage		Endocardium ADM		Endocardium APD	
		Testing	Online	Testing	Online	Testing	Online
MV	LB	91.08(15.11)	90.32(14.64)	0.87(0.05)	0.88(0.05)	2.77(0.53)	2.73(0.56)
PB	LB	92.11(12.00)	91.71(14.20)	0.87(0.06)	0.88(0.05)	2.76(0.54)	2.65(0.55)
SVMAF	LB	94.79(11.06)	92.86(12.65)	0.88(0.04)	0.89(0.05)	3.00(0.51)	2.82(0.60)
DBNLS	-	95.91(5.28)	90.54(14.40)	0.88(0.03)	0.89(0.03)	2.34(0.46)	2.17(0.46)
DBNLS(semiauto)	-	100(0)	100(0)	0.91(0.03)	0.91(0.03)	1.79(0.36)	1.78(0.49)
SAELS	-	97.8(4.7)	95.58(6.7)	0.94(0.02)	0.93(0.02)	1.7(0.37)	1.92(0.51)
SAELS(init)	-	90(10)	87(12)	0.90(0.1)	0.89(0.03)	2.84(0.29)	2.95(0.54)
DFN	LB	97.58(7.12)	96.36(8.41)	0.92(0.04)	0.92(0.03)	2.04(0.44)	2.06(0.58)
DFN	LF	73.56(29.00)	60.87(26.48)	0.91(0.06)	0.93(0.02)	2.31(0.40)	2.41(0.47)
DFN(multi)	LB	96.96(8.48)	95.70(9.12)	0.92(0.04)	0.92(0.03)	2.01(0.42)	2.04(0.58)
DFN_NMI	LB	97.25(7.24)	95.41(9.43)	0.92(0.04)	0.92(0.04)	2.05(0.42)	2.04(0.53)
DFN_NMI	LF	66.61(29.59)	53.81(25.88)	0.92(0.03)	0.90(0.07)	2.35(0.47)	2.66(0.65)
DFN_NMI(multi)	LB	97.44(7.32)	94.99(10.05)	0.92(0.04)	0.92(0.04)	2.06(0.41)	2.02(0.50)

Table 3: Endocardium segmentation accuracies of different methods on testing and online sets of LV-09 dataset, where only training set is used as training data. Each cell is formatted as “mean (standard deviation)”.

net is trained for endocardium at ES. Notice that DBNLS respectively utilizes training set for model training and online set for model selection, and reports the performance on testing set, while SAELS has the same experimental setting with us, *i.e.*, training on training set and reporting results on testing and online sets. Since SAELS has not been evaluated on epicardium in Avendi et al. (2016), we only compare its accuracy on endocardium segmentation in Table 3.

As shown in Tables 2 and 3, our DFN performs better than the other registration-based methods (*i.e.*, MV, PB and SVMAF) on epicardium and endocardium segmentations in all metrics (p -value < 0.001) when using LB registration. In comparison with the deep learning-based methods, the only method that outperforms our DFN is DBNLS but only when it utilizes the strong manual prior (*i.e.*, manually-labeled segmentation masks as prior, referred as DBNLS(semiauto)). In fact, compared to DBNLS without using the manual prior (referred as DBNLS), our DFN based on LB registration achieves much higher accuracies in all metrics. As for SAELS, our DFN using LB registration achieves comparable results on endocardium segmentation. However, SAELS utilizes post-processing to refine the initial segmentation of stacked autoencoder by level set method. Without post-processing, SAELS reports the ADM scores of 0.90 in testing set and 0.89 in online set, compared with 0.92 and 0.92 of ours purely based on thresholding the estimated label probability maps of deep fusion nets, as shown in Table 3. Compared with training separate DFN (referred as DFN), the multi-class DFN produces worse APD scores for epicardium (p -value < 0.001) and is comparable in other metrics.

Our DFN and DFN_NMI based on LF registration achieve lower values of “Good” percentage in all comparisons, due to the inaccurate registration results without using landmarks on this dataset. This indicates that our method,

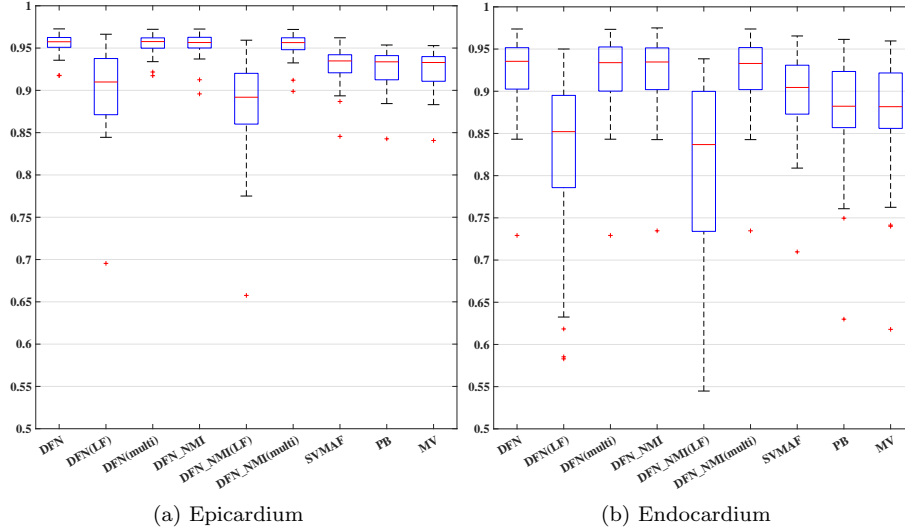


Fig. 7: Comparison of (a) epicardium and (b) endocardium segmentation accuracies for different methods on LV-09 dataset in averaged 3D Dice metric (ADM). The ADM are averaged over all testing subjects. The red central mark of the box is the median and the edges are the 25th and 75th percentiles, while the red plus signs represent outliers.

as a multi-atlas segmentation method, relies on a relatively good registration method, and breaks down on LV-09 dataset when LF registration does not work well. Figure 7 compares the segmentation accuracies in the box-plot, and Figure 8 shows the epicardium and endocardium segmentation results using different methods for the basal, mid-ventricular and apical slices from one subject in testing set.

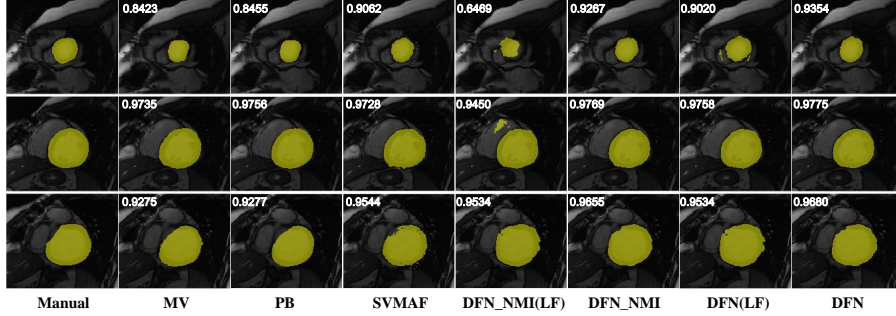
4.5. Evaluation on network architecture

4.5.1. Impact of sigmoid layer

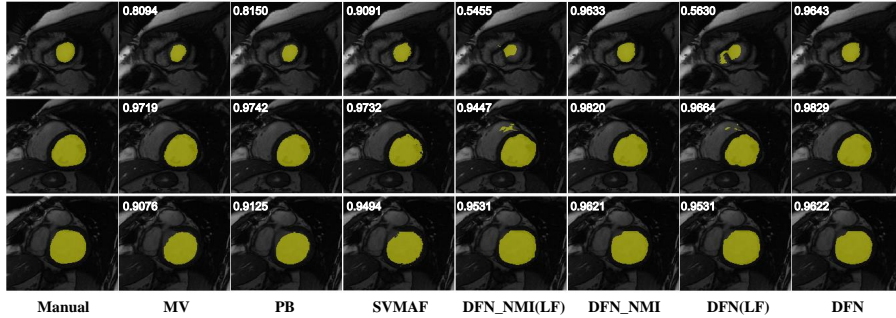
In the feature extraction subnet discussed in section 2.2, we added a sigmoid layer at the end of this subnet to suppress the magnitudes of deep features for robustness, and its outputs are taken as voxel-wise features for computing label fusion weights. We now experimentally evaluate the necessity of sigmoid layer on segmentation performance.

First, we train two deep fusion nets with or without sigmoid layer for epicardium at ED frame using 15 training subjects, and test on 30 testing and online subjects of LV-09 database. The testing accuracies are reported in Table 4. The results show that the network with sigmoid layer is better than the one without sigmoid layer in “Good” percentage (p -value < 0.05) and APD (p -value < 0.001) with comparable ADM, indicating the effectiveness of the sigmoid layer on improving the segmentation accuracies.

Second, we also evaluate the performance of learned deep features with and without sigmoid layer as similarity measure. We compare the majority voting



(a) Epicardium segmentation results at ED frame.



(b) Endocardium segmentation results at ED frame.

Fig. 8: Visual comparison of segmentation results using different methods on LV-09 dataset. Epicardium slices in (a) and endocardium slices in (b) are from one subject at testing set. Please refer to the electronic version for better comparison. Top to bottom: the basal, mid-ventricular and apical slices from the same subject. Left to right: manual labeling, majority voting (MV), patch-based method (PB), SVM segmentation with augmented features (SVMAF), DFN_NMI using LF registration, DFN_NMI, DFN using LF registration, and DFN. The small white text in each sub-image is the corresponding 2D Dice metric value.

Normalization	“Good” percentage	ADM	APD
DFN (w/ sigmoid)	97.59(6.18)	0.9499(0.01)	1.97(0.30)
DFN (w/o sigmoid)	94.49(11.80)	0.9464(0.01)	2.15(0.43)

Table 4: Epicardium segmentation accuracies of deep fusion nets with or without sigmoid layer at ED frame on testing and online sets of LV-09 dataset. The number of selected atlases is fixed as 5 for both training and testing. Each cell is formatted as “mean (standard deviation)”.

Similarity	“Good” percentage	ADM	APD
Deep features (w/ sigmoid)	84.39(13.18)	0.9056(0.02)	3.03(0.50)
Deep features (w/o sigmoid)	79.37(16.19)	0.9012(0.02)	3.25(0.47)
NMI	74.65(15.31)	0.9087(0.02)	3.07(0.54)

Table 5: Epicardium segmentation accuracies of majority voting using different atlas selection strategies at ED frame on testing and online sets of LV-09 dataset. Atlas selection is implemented respectively using NMI, deep features learned with and without sigmoid layer. Each cell is formatted as “mean (standard deviation)”.

methods respectively using deep features learned by deep fusion nets with sigmoid layer (referred as Deep features (w/ sigmoid)) or without sigmoid layer (referred as Deep features (w/o sigmoid)), and normalized mutual information (referred as NMI) as similarity measures on epicardium segmentation at ED frame of LV-09 database. Only training set is used as atlases, and the testing accuracies are computed in testing and online sets. The results are listed in Table 5, showing that deep features learned with sigmoid layer work better than the ones learned without sigmoid layer and NMI in “Good” percentage (p -value < 0.05) with comparable ADM and APD.

4.5.2. Impact of loss layer

In this experiment, we compare the performance of our methods using 5 different loss functions, *i.e.*, L_2 , L_1 , hinge (Cortes and Vapnik, 1995), Dice (Milletari et al., 2016) and log (Murphy, 2012) losses. We train 5 different networks for epicardium at ED using 15 training subjects, and test on 30 testing and online subjects of LV-09 database. The learning rates are tuned such that the loss can decently decrease. The testing accuracies reported in Table 6 show that L_2 loss achieves marginally better accuracies compared with some traditional segmentation losses, *e.g.*, hinge, Dice and log losses. We failed to train a converged parameter set for deep fusion net using cross-entropy loss, which seems to be counter-intuitive. But due to the specially designed linear voting layer

Loss	“Good” percentage	ADM	APD
L_2	97.59(6.18)	0.9499(0.01)	1.97(0.30)
L_1	97.39(9.41)	0.9503(0.01)	2.00(0.34)
Hinge	96.90(8.19)	0.9490(0.01)	2.04(0.36)
Dice	96.75(9.27)	0.9475(0.01)	2.03(0.37)
Log	95.61(10.25)	0.9486(0.01)	2.05(0.34)

Table 6: Epicardium segmentation accuracies of deep fusion nets with different loss layers at ED frame on testing and online sets of LV-09 dataset. The number of selected atlases is fixed as 5 for both training and testing. Each cell is formatted as “mean (standard deviation)”.

R_{nl}	“Good” percentage	ADM	APD
[1, 1]	97.35(6.50)	0.9418(0.01)	2.17(0.36)
[3, 3]	96.15(11.72)	0.9453(0.01)	2.10(0.35)
[5, 5]	96.03(9.47)	0.9483(0.01)	1.96(0.30)
[7, 7]	97.59(6.18)	0.9499(0.01)	1.97(0.30)
[9, 9]	97.89(6.06)	0.9507(0.01)	1.94(0.32)

Table 7: Epicardium segmentation accuracies by training DFNs with different sizes of search volumes R_{nl} on training set and testing on testing and online sets of LV-09 dataset. The number of selected atlases is fixed as 5 for both training and testing. Each cell is formatted as “mean (standard deviation)”.

before the loss layer, the cross-entropy loss causes unstable gradients for error back-propagation in network training (please refer to section 2.3).

4.5.3. Impact of search volume

We now evaluate the influence of search volume R_{nl} , *i.e.*, the non-local region for patch-based label fusion, on the segmentation performance. As shown in Table 7, we respectively train five DFNs with different search volumes, whose sizes range from 1 to 9 with interval of 2, on epicardium at ED frame using 15 training subjects, and test on 30 testing and online subjects of LV-09 dataset. The results indicate that the segmentation accuracies are not sensitive to search volume, and generally a larger size of search volume could produce marginally better segmentation accuracies. This is reasonable since larger search volume provides more patch candidates around registered pixels for label fusion, resulting in robustness to inaccurate registrations.

4.6. Comparison on atlas selection strategy

In the training and testing phases of our DFNs, we could choose different atlas selection strategies, *e.g.*, selecting different numbers of atlases, using either deep feature distance or NMI for atlas selection. In this section, we will test the impacts of different atlas selection strategies on the performance of DFN.

We first compare the segmentation accuracies of our proposed methods (referred to DFN_NMI and DFN) with respect to different numbers of selected atlases at testing phase. The deep fusion nets learned in sections 4.4.1 and 4.4.2, which use randomly selected 5 atlases according to a distribution proportional to NMI between target image and atlases at training phase, are utilized in this comparison. As shown in Fig. 9, we compare the performance of DFN_NMI and DFN on SATA-13 dataset (Fig. 9a and 9b) and LV-09 dataset (Fig. 9c and 9d) respectively. The experimental results show that atlas selection using deep feature distance consistently works better than that using NMI for different numbers of selected atlases at testing phase. Moreover, using larger numbers of atlases generally produces better ADM scores, but the accuracies saturate after around 11 atlases.

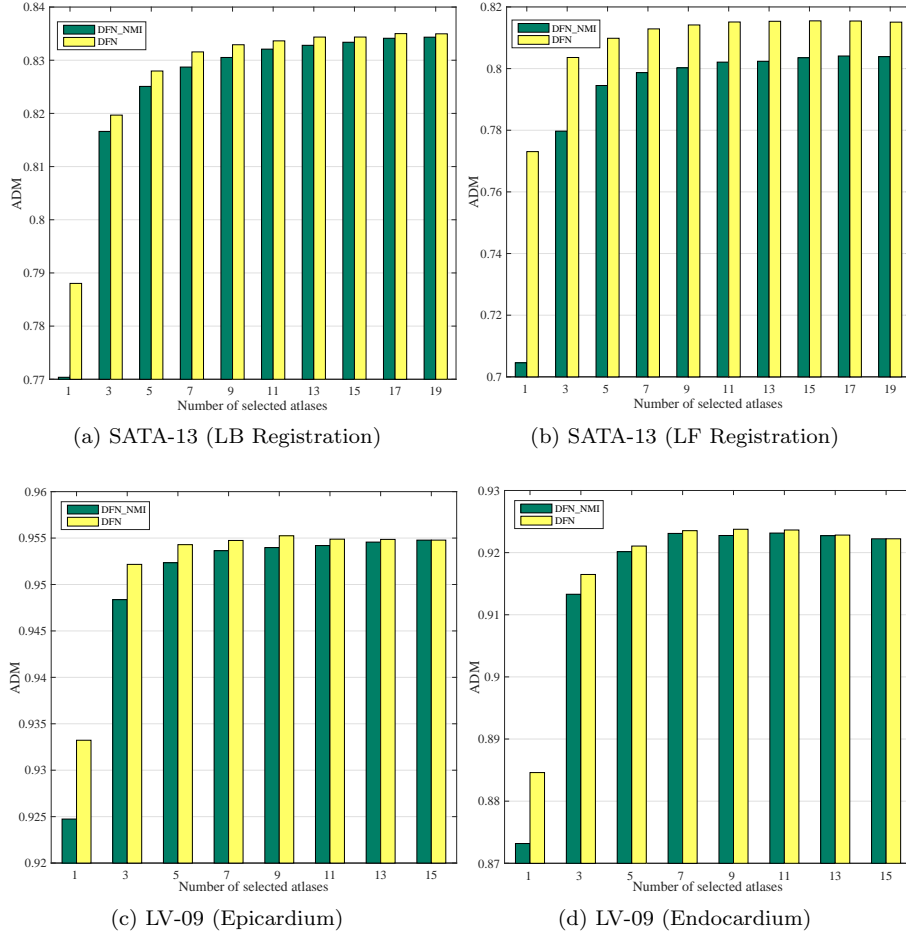


Fig. 9: The change of averaged 3D Dice metric (ADM) *w.r.t.* the number of selected atlases at testing process. The ADM are averaged over all testing subjects. (a) and (b) are respectively using LB registration and LF registration for myocardium segmentation on SATA-13 dataset, while (c) and (d) are for epicardium and endocardium segmentations utilizing LB registration on LV-09 dataset.

Training	Testing	“Good” percentage	ADM	APD
Random5_NMI	Top5_DF	97.59(6.18)	0.9499(0.01)	1.97(0.30)
	Top5_NMI	95.71(9.34)	0.9503(0.01)	2.01(0.30)
Top5_DF	Top5_DF	97.40(6.46)	0.9483(0.01)	2.00(0.33)
	Top5_NMI	94.59(10.26)	0.9488(0.01)	2.03(0.29)
Top5_NMI	Top5_DF	96.90(8.99)	0.9468(0.01)	2.02(0.32)
	Top5_NMI	95.30(10.51)	0.9472(0.01)	2.05(0.33)

Table 8: Epicardium segmentation accuracies of DFNs with different atlas selection strategies at training and testing phases on testing and online sets of LV-09 dataset, where only training set is used as training data. Each cell is formatted as “mean (standard deviation)”.

We next experimentally investigate the advantages of our random atlas selection strategy at training phase, which has been discussed in section 2.5. By fixing the number of selected atlases to 5, we compare the performance of DFNs using three different atlas selection strategies in each forward-backward computation of training process, *i.e.*, selecting top-5 atlases with smallest deep feature distances (top5_DF), selecting top-5 atlases with largest normalize mutual information (top5_NMI), and randomly selecting atlases according to a distribution proportional to NMI between target and atlas images (random5_NMI). We train DFNs with the above strategies for epicardium at ED using 15 training subjects, and test on 30 testing and online subjects of LV-09 dataset. For each strategy at training phase, we attempt two different atlas selection strategies at testing phase, *i.e.*, select top-5 atlases with largest normalize mutual information (top5_NMI) and select top-5 atlases with smallest deep feature distance (top5_DF). The experimental results are listed in Table 8. Compared with the strategies of top5_DF and top5_NMI at training phase, the strategy of using random5_NMI performs best in all metrics. Moreover, random5_NMI paired with top5_DF strategies at training and testing phases achieves the best accuracies

K_0	“Good” percentage	ADM	APD
1	95.66(9.60)	0.9335(0.02)	2.34(0.50)
3	97.17(6.43)	0.9463(0.01)	2.07(0.37)
5	97.59(6.18)	0.9499(0.01)	1.97(0.30)
7	97.14(8.78)	0.9499(0.01)	1.93(0.29)
9	96.25(10.00)	0.9496(0.01)	1.97(0.29)

Table 9: Epicardium segmentation accuracies by training DFNs with different numbers of selected atlases K_0 on training set and testing on testing and online sets of LV-09 dataset. The size of search volume is fixed as [7,7], and the number of selected atlases for testing is same as the corresponding training one. Each cell is formatted as “mean (standard deviation)”.

among all the compared strategies.

In Table 9, we also compare the performance of DFN by varying the numbers of selected atlases (denoted as K_0) at training phase using random atlas selection strategy, with K_0 atlases selected by deep feature distance at testing phase. The experimental results show that the segmentation accuracies are relatively stable to K_0 , *e.g.*, the accuracies are not significantly lower even when using 1 training atlas (*i.e.*, $K_0 = 1$). This is probably because the random atlas selection strategy enforces that each target image at training phase can be paired with diverse atlases. Empirically, K_0 with values of 5 to 7 produces best accuracies.

4.7. Cross-dataset evaluation

To evaluate the generalization abilities of the learned DFNs across different datasets, we conduct experimental comparisons for network training and testing across two different datasets. More specifically, we train each DFN on one dataset and test it on the other one. When we test the DFN learned from training dataset on the testing dataset, we attempt two different atlas selection strategies for the testing subjects, *i.e.*, selecting atlases from the subjects in the training dataset or in the testing dataset. We create the segmentation mask of myocardium for LV-09 dataset by subtracting the endocardium mask from the epicardium mask, to be compatible with the ground-truth segmentation mask provided in SATA-13 dataset. The experiments are performed on ED frame of both datasets, and the accuracy is evaluated by averaged 3D Dice metric (ADM) and averaged 3D Hausdorff distance (AHD) over all subjects at ED frame of the testing dataset.

We first evaluate the cross-dataset performance using the strategy that selects atlases from the subjects in the training dataset for the testing subjects in the testing dataset, and the segmentation accuracies are listed in Table 10 (train DFN on LV-09 and test it on SATA-13) and Table 11 (train DFN on SATA-13 and test it on LV-09). The experimental results show that our learned DFNs achieve significantly higher ADMs (p -value < 0.001) and marginally better AHDs than traditional multi-atlas segmentation methods on both two datasets. Compared with the methods that perform training and testing on

Method	Averaged Dice metric	Averaged Hausdorff distance
MV	0.620(0.066)	16.58(3.22)
PB	0.639(0.067)	16.69(3.26)
SVMAF	0.691(0.082)	22.15(5.82)
DFN	0.734(0.058)	15.32(3.88)
DFN_NMI	0.730(0.060)	15.82(4.44)

Table 10: Myocardium segmentation results by training DFNs on LV-09 dataset and testing on SATA-13 dataset, where 45 subjects of LV-09 dataset are used as atlases in the testing process. Each cell is formatted as “mean (standard deviation)”.

Method	Averaged Dice metric	Averaged Hausdorff distance
MV	0.672(0.057)	11.83(3.10)
PB	0.681(0.055)	11.45(2.55)
SVMAF	0.708(0.044)	17.63(4.93)
DFN	0.766(0.042)	10.68(3.84)
DFN_NMI	0.763(0.044)	11.95(4.78)

Table 11: Myocardium segmentation results by training DFNs on SATA-13 dataset and testing on LV-09 dataset, where 83 subjects of SATA-13 dataset are used as atlases in the testing process. Each cell is formatted as “mean (standard deviation)”.

the same dataset, *e.g.*, Table 1 in section 4.4.1, the accuracies of our DFN for cross-dataset evaluation are relatively low, which is possibly because of the different styles of manual labels in these two datasets, as shown in Fig. 10 (please refer to the figure for detailed descriptions of this difference). Figure 11 shows the performance of deep fusion nets using different numbers of selected atlases respectively on two datasets in the testing process, indicating that our defined deep feature distance consistently works better than NMI in all metrics.

We also evaluate the cross-dataset performance using the strategy that selects atlases from the subjects in the testing dataset for testing subjects. In Table 1, we present the results of our methods (denoted as DFN(crossDS) and DFN_NMI(crossDS)) by applying the DFN learned from LV-09 dataset to the SATA-13 dataset without fine-tuning. These accuracies are calculated using the same 5-fold cross validation utilized in section 4.4.1. The experimental results show that, if the subjects in SATA-13 dataset are used as atlases for testing subjects, the DFN learned from LV-09 dataset can achieve comparable results on SATA-13 dataset in all metrics, compared with those segmentation meth-

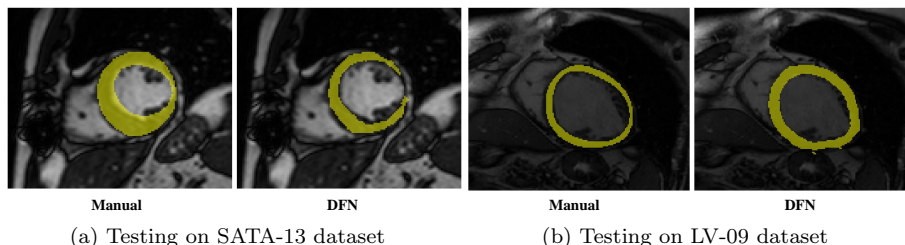
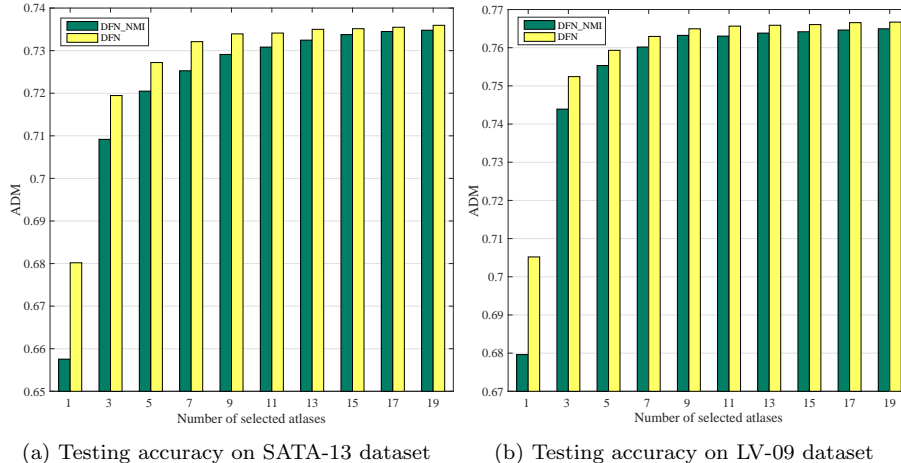


Fig. 10: Visual examples of estimated myocardium segmentations by DFN (right) and corresponding manual segmentations (left) in (a) SATA-13 dataset and (b) LV-09 dataset. As we can see, manual segmentation in (a) SATA-13 dataset is much “thicker” than the one in (b) LV-09 dataset. In (b) LV-09 dataset, the estimated segmentation by DFN is much “thicker” than the manual one, possibly because the network here is trained on “thick” labels of SATA-13 dataset and utilizes “thick” atlases to estimate the target label. Similarly, the estimated segmentation in (a) SATA-13 dataset is much “thinner” than the manual one.



(a) Testing accuracy on SATA-13 dataset (b) Testing accuracy on LV-09 dataset

Fig. 11: The change of averaged 3D Dice metric (ADM) *w.r.t.* the number of selected atlases respectively on (a) SATA-13 dataset and (b) LV-09 dataset for myocardium segmentation at testing phase. The ADM are averaged over all testing subjects.

ods training and testing on the same SATA-13 dataset. This justifies that our learned feature extraction subnet has well generalization ability across different datasets for LV segmentation.

5. Conclusions

In this work, we accomplish the multi-atlas based LV segmentation by a specially designed convolutional neural network. Our network relies on atlas-to-target image registration, and aims to extract deep features for optimally fusing the warped atlas labels in a non-local patch-based label fusion framework. This deep fusion net naturally bridges the traditional registration-based multi-atlas approach and modern deep learning approach, and provides a novel deep architecture for solving the tasks of label fusion and atlas selection in multi-atlas segmentation approach. The proposed net was evaluated SATA-13 and LV-09 datasets for LV segmentation, and the results demonstrate that it achieves better accuracies in various metrics than the other LV segmentation methods on both datasets, and the only method surpassing ours is the deep learning method using a strong manual prior (Ngo et al., 2017). We also extensively evaluate the performance of deep fusion nets using variants of architecture, training loss, atlas selection strategy, cross-dataset training and testing, *etc.*

As a registration-based multi-atlas segmentation method, our deep fusion net relies on a good image registration method, and may fail when the atlas-to-target image registration is not accurate enough. For example, our deep fusion net using landmark-free registration works well on SATA-13 dataset while producing unsatisfactory results on LV-09 dataset. To improve its robustness

to registration errors, first, larger search volume can be utilized to incorporate more voxels around registered voxel for label fusion. Second, it is interesting to build a more robust label fusion subnet for multi-atlas segmentation via the statistical fusion strategy. Moreover, our present study is based on 2D slices mainly due to the constraint of GPU memory. This is also a common issue for deep learning approaches when applied to 3D medical images. One common solution is to train the networks using 3D patches instead of full 3D images (Kamnitsas et al., 2017; Dou et al., 2017).

In the future work, we are interested in improving the label fusion subnet by investigating more robust statistical fusion strategy, and applying the proposed framework to 3D images. As a general framework, our deep fusion net can also be applied to other multi-atlas based applications, *e.g.*, image synthesis (Roy et al., 2013), brain segmentation (Asman et al., 2015), *etc.*

Acknowledgments

This work was supported by the National Natural Science Foundation of China (NSFC) under Grant No. 11622106, 61472313, 11690011 and 61721002, International Exchange Foundation of China NSFC and United Kingdom RS under grant No. 61711530242.

References

References

- Aljabar, P., Heckemann, R., Hammers, A., Hajnal, J., Rueckert, D., 2009. Multi-atlas based segmentation of brain images: Atlas selection and its effect on accuracy. *NeuroImage* 46, 726 – 738. doi:10.1016/j.neuroimage.2009.02.018.
- Artaechevarria, X., Munoz-Barrutia, A., de Solorzano, C.O., 2009. Combination strategies in multi-atlas image segmentation: Application to brain MR data. *IEEE Transactions on Medical Imaging* 28, 1266–1277. doi:10.1109/TMI.2009.2014372.
- Asman, A.J., Huo, Y., Plassard, A.J., Landman, B.A., 2015. Multi-atlas learner fusion: An efficient segmentation approach for large-scale data. *Medical Image Analysis* 26, 82 – 91. doi:10.1016/j.media.2015.08.010.
- Asman, A.J., Landman, B.A., 2013. Non-local statistical label fusion for multi-atlas segmentation. *Medical Image Analysis* 17, 194 – 208. doi:10.1016/j.media.2012.10.002.
- Avendi, M., Kheradvar, A., Jafarkhani, H., 2016. A combined deep-learning and deformable-model approach to fully automatic segmentation of the left ventricle in cardiac MRI. *Medical Image Analysis* 30, 108 – 119. doi:10.1016/j.media.2016.01.005.

- Bai, W., Shi, W., Ledig, C., Rueckert, D., 2015. Multi-atlas segmentation with augmented features for cardiac MR images. *Medical image analysis* 19, 98–109. doi:10.1016/j.media.2014.09.005.
- Bai, W., Shi, W., O’Regan, D.P., Tong, T., Wang, H., Jamil-Copley, S., Peters, N.S., Rueckert, D., 2013. A probabilistic patch-based label fusion model for multi-atlas segmentation with registration refinement: Application to cardiac MR images. *IEEE Transactions on Medical Imaging* 32, 1302–1315. doi:10.1109/TMI.2013.2256922.
- BenTaieb, A., Hamarneh, G., 2016. Topology aware fully convolutional networks for histology gland segmentation, in: Ourselin, S., Joskowicz, L., Sabuncu, M.R., Unal, G., Wells, W. (Eds.), *Medical Image Computing and Computer-Assisted Intervention (MICCAI) 2016*, pp. 460–468.
- Cardoso, M.J., Leung, K., Modat, M., Keihaninejad, S., Cash, D., Barnes, J., Fox, N.C., Ourselin, S., 2013. STEPS: Similarity and truth estimation for propagated segmentations and its application to hippocampal segmentation and brain parcellation. *Medical Image Analysis* 17, 671 – 684. doi:10.1016/j.media.2013.02.006.
- Chen, H., Qi, X., Yu, L., Dou, Q., Qin, J., Heng, P.A., 2017. DCAN: Deep contour-aware networks for object instance segmentation from histology images. *Medical Image Analysis* 36, 135 – 146. doi:10.1016/j.media.2016.11.004.
- Chopra, S., Hadsell, R., LeCun, Y., 2005. Learning a similarity metric discriminatively, with application to face verification, in: *IEEE CVPR 2005*, pp. 539–546. doi:10.1109/CVPR.2005.202.
- Collignon, A., Maes, F., Delaere, D., Vandermeulen, D., Suetens, P., Marchal, G., 1995. Automated multi-modality image registration based on information theory, in: Bizais, Y., Barillot, C., Paola, R. (Eds.), *Information Processing in Medical Imaging (IPMI) 1995*, Kluwer Academic Publishers, Dordrecht. pp. 263–274.
- Commowick, O., Warfield, S.K., Malandain, G., 2009. Using Frankenstein’s creature paradigm to build a patient specific atlas, in: *Medical Image Computing and Computer-Assisted Intervention (MICCAI) 2009*, Springer Berlin Heidelberg. pp. 993–1000. doi:10.1007/978-3-642-04271-3_120.
- Cortes, C., Vapnik, V., 1995. Support-vector networks. *Machine Learning* 20, 273–297. doi:10.1007/BF00994018.
- Coupé, P., Manjón, J.V., Fonov, V., Pruessner, J., Robles, M., Collins, D.L., 2011. Patch-based segmentation using expert priors: Application to hippocampus and ventricle segmentation. *NeuroImage* 54, 940 – 954. doi:10.1016/j.neuroimage.2010.09.018.

- Dou, Q., Yu, L., Chen, H., Jin, Y., Yang, X., Qin, J., Heng, P.A., 2017. 3D deeply supervised network for automated segmentation of volumetric medical images. *Medical Image Analysis* 41, 40–54. doi:10.1016/j.media.2017.05.001.
- Duc, A.K.H., Modat, M., Leung, K.K., Cardoso, M.J., Barnes, J., Kadir, T., Ourselin, S., Initiative, A.D.N., 2013. Using manifold learning for atlas selection in multi-atlas segmentation. *PLoS ONE* 8, 1–11. doi:10.1371/journal.pone.0070059.
- Fu, H., Xu, Y., Lin, S., Kee Wong, D.W., Liu, J., 2016. DeepVessel: Retinal vessel segmentation via deep learning and conditional random field, in: *Medical Image Computing and Computer-Assisted Intervention (MICCAI) 2016*, Springer International Publishing. pp. 132–139. doi:10.1007/978-3-319-46723-8_16.
- Goodfellow, I., Bengio, Y., Courville, A., 2016. *Deep Learning*. MIT Press. URL: www.deeplearningbook.org.
- Guo, Y., Gao, Y., Shen, D., 2016. Deformable MR prostate segmentation via deep feature learning and sparse patch matching. *IEEE Transactions on Medical Imaging* 35, 1077–1089. doi:10.1109/TMI.2015.2508280.
- Havaei, M., Davy, A., Warde-Farley, D., Biard, A., Courville, A., Bengio, Y., Pal, C., Jodoin, P.M., Larochelle, H., 2017. Brain tumor segmentation with deep neural networks. *Medical Image Analysis* 35, 18 – 31. doi:10.1016/j.media.2016.05.004.
- Heckemann, R.A., Hammers, A., Aljabar, P., Rueckert, D., Hajnal, J.V., 2009. The mirror method of assessing segmentation quality in atlas label propagation, in: *International Symposium on Biomedical Imaging (ISBI) 2009*, pp. 1194–1197. doi:10.1109/ISBI.2009.5193272.
- Iglesias, J.E., Sabuncu, M.R., 2015. Multi-atlas segmentation of biomedical images: a survey. *Medical image analysis* 24, 205–219.
- Kamnitsas, K., Ledig, C., Newcombe, V.F., Simpson, J.P., Kane, A.D., Menon, D.K., Rueckert, D., Glocker, B., 2017. Efficient multi-scale 3D CNN with fully connected CRF for accurate brain lesion segmentation. *Medical Image Analysis* 36, 61 – 78. doi:10.1016/j.media.2016.10.004.
- Khalaf, A.F., Yassine, I.A., Fahmy, A.S., 2016. Convolutional neural networks for deep feature learning in retinal vessel segmentation, in: *International Conference on Image Processing (ICIP) 2016*, pp. 385–388. doi:10.1109/ICIP.2016.7532384.
- Krizhevsky, A., Sutskever, I., Hinton, G.E., 2012. Imagenet classification with deep convolutional neural networks, in: *Advances in neural information processing systems*, pp. 1097–1105.

- Landman, B., Warfield, S., 2013. 2013 Cardiac Atlas Project Free Challenge. doi:10.7303/syn3270357.
- Litjens, G., Kooi, T., Bejnordi, B.E., Setio, A.A.A., Ciampi, F., Ghafoorian, M., van der Laak, J.A., van Ginneken, B., Sánchez, C.I., 2017. A survey on deep learning in medical image analysis. *Medical image analysis* 42, 60–88. doi:10.1016/j.media.2017.07.005.
- Makropoulos, A., Gousias, I.S., Ledig, C., Aljabar, P., Serag, A., Hajnal, J.V., Edwards, A.D., Counsell, S.J., Rueckert, D., 2014. Automatic whole brain MRI segmentation of the developing neonatal brain. *IEEE Transactions on Medical Imaging* 33, 1818–1831. doi:10.1109/TMI.2014.2322280.
- Maninis, K.K., Pont-Tuset, J., Arbeláez, P., Van Gool, L., 2016. Deep retinal image understanding, in: *Medical Image Computing and Computer-Assisted Intervention (MICCAI) 2016*, Springer International Publishing. pp. 140–148. doi:10.1007/978-3-319-46723-8_17.
- Milletari, F., Navab, N., Ahmadi, S.A., 2016. V-net: Fully convolutional neural networks for volumetric medical image segmentation, in: *2016 Fourth International Conference on 3D Vision (3DV)*, pp. 565–571. doi:10.1109/3DV.2016.79.
- Moeskops, P., Viergever, M.A., Mendrik, A.M., de Vries, L.S., Benders, M.J.N.L., Igum, I., 2016. Automatic segmentation of MR brain images with a convolutional neural network. *IEEE Transactions on Medical Imaging* 35, 1252–1261. doi:10.1109/TMI.2016.2548501.
- Murphy, K.P., 2012. *Machine learning: a probabilistic perspective*. Cambridge, MA.
- Nair, V., Hinton, G.E., 2010. Rectified linear units improve restricted boltzmann machines, in: *27th international conference on machine learning (ICML-10)*, pp. 807–814.
- Ngo, T.A., Lu, Z., Carneiro, G., 2017. Combining deep learning and level set for the automated segmentation of the left ventricle of the heart from cardiac cine magnetic resonance. *Medical Image Analysis* 35, 159 – 171. doi:10.1016/j.media.2016.05.009.
- Petitjean, C., Dacher, J.N., 2011. A review of segmentation methods in short axis cardiac MR images. *Medical Image Analysis* 15, 169 – 184. doi:10.1016/j.media.2010.12.004.
- Radau, P., Lu, Y., Connelly, K., Paul, G., Dick, A., Wright, G., 2009. Evaluation framework for algorithms segmenting short axis cardiac MRI. *Midas Journal* URL: <http://hdl.handle.net/10380/3070>.

- Rajchl, M., Lee, M.C.H., Oktay, O., Kamnitsas, K., Passerat-Palmbach, J., Bai, W., Damodaram, M., Rutherford, M.A., Hajnal, J.V., Kainz, B., Rueckert, D., 2017. DeepCut: Object segmentation from bounding box annotations using convolutional neural networks. *IEEE Transactions on Medical Imaging* 36, 674–683. doi:10.1109/TMI.2016.2621185.
- Ronneberger, O., Fischer, P., Brox, T., 2015. U-Net: Convolutional networks for biomedical image segmentation, in: Navab, N., Hornegger, J., Wells, W.M., Frangi, A.F. (Eds.), *Medical Image Computing and Computer-Assisted Intervention (MICCAI) 2015*, Springer International Publishing. pp. 234–241. doi:10.1007/978-3-319-24574-4_28.
- Roy, S., Carass, A., Prince, J.L., 2013. Magnetic resonance image example-based contrast synthesis. *IEEE Transactions on Medical Imaging* 32, 2348–2363. doi:10.1109/TMI.2013.2282126.
- Sanroma, G., Wu, G., Gao, Y., Shen, D., 2014. Learning to rank atlases for multiple-atlas segmentation. *IEEE Transactions on Medical Imaging* 33, 1939–1953. doi:10.1109/TMI.2014.2327516.
- Sanroma, G., Wu, G., Gao, Y., Thung, K.H., Guo, Y., Shen, D., 2015. A transversal approach for patch-based label fusion via matrix completion. *Medical Image Analysis* 24, 135 – 148. doi:10.1016/j.media.2015.06.002.
- Schroff, F., Kalenichenko, D., Philbin, J., 2015. FaceNet: A unified embedding for face recognition and clustering, in: *Computer Vision and Pattern Recognition (CVPR) 2015*, pp. 815–823. doi:10.1109/CVPR.2015.7298682.
- Shi, W., Lombaert, H., Bai, W., Ledig, C., Zhuang, X., Marvao, A., Dawes, T., O’Regan, D., Rueckert, D., 2014. Multi-atlas spectral patchmatch: Application to cardiac image segmentation, in: *Medical Image Computing and Computer-Assisted Intervention (MICCAI) 2014*, pp. 348–355. doi:10.1007/978-3-319-10404-1_44.
- Srivastava, N., Hinton, G., Krizhevsky, A., Sutskever, I., Salakhutdinov, R., 2014. Dropout: A simple way to prevent neural networks from overfitting. *Journal of Machine Learning Research* 15, 1929–1958.
- Studholme, C., Hill, D., Hawkes, D., 1999. An overlap invariant entropy measure of 3D medical image alignment. *Pattern Recognition* 32, 71 – 86. doi:10.1016/S0031-3203(98)00091-0.
- Tong, T., Wolz, R., Wang, Z., Gao, Q., Misawa, K., Fujiwara, M., Mori, K., Hajnal, J.V., Rueckert, D., 2015. Discriminative dictionary learning for abdominal multi-organ segmentation. *Medical Image Analysis* 23, 92 – 104. doi:10.1016/j.media.2015.04.015.
- Vincent, P., Larochelle, H., Bengio, Y., Manzagol, P.A., 2008. Extracting and composing robust features with denoising autoencoders, in: *International Conference on Machine Learning (ICML) 2008*, pp. 1096–1103. doi:10.1145/1390156.1390294.

- Wachinger, C., Reuter, M., Klein, T., 2017. DeepNAT: Deep convolutional neural network for segmenting neuroanatomy. *NeuroImage* doi:10.1016/j.neuroimage.2017.02.035.
- Wang, H., Suh, J.W., Das, S.R., Pluta, J.B., Craige, C., Yushkevich, P.A., 2013. Multi-atlas segmentation with joint label fusion. *IEEE Transactions on Pattern Analysis and Machine Intelligence* 35, 611–623. doi:10.1109/TPAMI.2012.143.
- Wang, Z., Bhatia, K.K., Glocker, B., Marvao, A., Dawes, T., Misawa, K., Mori, K., Rueckert, D., 2014. Geodesic patch-based segmentation, in: *Medical Image Computing and Computer-Assisted Intervention (MICCAI) 2014*, Springer International Publishing. pp. 666–673. doi:10.1007/978-3-319-10404-1_83.
- Warfield, S.K., Zou, K.H., Wells, W.M., 2004. Simultaneous truth and performance level estimation (STAPLE): an algorithm for the validation of image segmentation. *IEEE Transactions on Medical Imaging* 23, 903–921. doi:10.1109/TMI.2004.828354.
- Wolz, R., Chu, C., Misawa, K., Fujiwara, M., Mori, K., Rueckert, D., 2013. Automated abdominal multi-organ segmentation with subject-specific atlas generation. *IEEE Transactions on Medical Imaging* 32, 1723–1730. doi:10.1109/TMI.2013.2265805.
- Wu, G., Wang, Q., Zhang, D., Nie, F., Huang, H., Shen, D., 2014. A generative probability model of joint label fusion for multi-atlas based brain segmentation. *Medical Image Analysis* 18, 881 – 890. doi:10.1016/j.media.2013.10.013.
- Xie, L., Sedai, S., Liang, X., Compas, C.B., Wang, H., Yushkevich, P.A., Syeda-Mahmood, T., 2015. Multi-atlas label fusion with augmented atlases for fast and accurate segmentation of cardiac MR images, in: *International Symposium on Biomedical Imaging (ISBI) 2015*, pp. 376–379. doi:10.1109/ISBI.2015.7163891.
- Xu, Z., Burke, R.P., Lee, C.P., Baucom, R.B., Poulouse, B.K., Abramson, R.G., Landman, B.A., 2015. Efficient multi-atlas abdominal segmentation on clinically acquired CT with SIMPLE context learning. *Medical Image Analysis* 24, 18 – 27. doi:10.1016/j.media.2015.05.009.
- Yang, H., Sun, J., Li, H., Wang, L., Xu, Z., 2016. Deep fusion net for multi-atlas segmentation: Application to cardiac MR images, in: *Medical Image Computing and Computer-Assisted Intervention (MICCAI) 2016*, Springer International Publishing. pp. 521–528. doi:10.1007/978-3-319-46723-8_60.
- Zagoruyko, S., Komodakis, N., 2015. Learning to compare image patches via convolutional neural networks, in: *Computer Vision and Pattern Recognition (CVPR) 2015*, pp. 4353–4361. doi:10.1109/CVPR.2015.7299064.

- Zheng, Z., Zheng, L., Yang, Y., 2016. A discriminatively learned CNN embedding for person re-identification. CoRR abs/1611.05666. URL: arxiv.org/abs/1611.05666.
- Zhuang, X., Shen, J., 2016. Multi-scale patch and multi-modality atlases for whole heart segmentation of MRI. Medical Image Analysis 31, 77 – 87. doi:10.1016/j.media.2016.02.006.